14. Data Report: Permeability, Resistivity, and X-Ray Computed Tomography Measurements in Samples from the PACMANUS Hydrothermal System[1]

Gerardo J. Iturrino,[2] Richard A. Ketcham,[3] Lizet Christiansen,[4] and Greg Boitnott[5]

INTRODUCTION

Magmatic fluids, heat fluxes, and fluid/rock interactions associated with hydrothermal systems along spreading centers and convergent margins have a significant impact on the genesis of major sulfide deposits and biological communities. Circulation of hydrothermal fluids is one of the most fundamental processes associated with localized mineralization and is controlled by inherent porous and permeable properties of the ocean crust. Heat from magmatic intrusions drives circulation of seawater through permeable portions of the oceanic crust and upper mantle, discharging at the seafloor as both focused high-temperature (250°–400°C) fluids and diffuse lower-temperature (<250°C) fluids. This complex interaction between the circulating hydrothermal fluids and the oceanic basement greatly influences the physical properties and the composition of the crust (Thompson, 1983; Jacobson, 1992; Johnson and Semyan, 1994).

During Ocean Drilling Program (ODP) Leg 193, 13 holes were drilled in the PACMANUS hydrothermal system (Binns, Barriga, Miller, et al., 2002). The hydrothermal system consists of isolated hydrothermal deposits lined along the main crest of the Pual Ridge, a 500- to 700-m-high felsic neovolcanic ridge in the eastern Manus Basin. The principal drilling targets were the Snowcap (Site 1188) and Roman Ruins (Site 1189) active hydrothermal fields. Samples from these two sites were

G.J. Iturrino et al.
Data Report: Permeability, Resistivity, and CT Measurements

2

used for a series of permeability, electrical resistivity, and X-ray computed tomography measurements.

METHODS AND MATERIALS

Permeability and Electrical Resistivity Measurements

The nine minicore samples (diameter = 2.54 cm; length = 2 cm) studied were highly variable in terms of their permeabilities, porosities, textures, and physical properties (Table T1). Some were soft and crushed or collapsed during testing, while others were quite competent. All samples were saturated with a 31 g/L sea salt solution at room temperature using "sea salt" from Sigma Chemical Co. to produce the brine. Samples were saturated by suspending them in a vacuum over a cup of brine for 1 hr, placing them into the brine, and releasing the vacuum. The samples were then equilibrated with 60 cm^3 of the brine in individual polypropylene cups prior to testing. The differences between saturated and dry densities were used to infer porosity for each sample.

Permeability and electrical resistivity were measured using an Auto-Lab 1000 test system capable of automated hydraulic control of confining and pore pressures. The samples were placed in a dual electrical resistivity/permeability core holder, which allows permeability- and frequency-dependent complex impedance to be measured during the same experiment. A complex transient method was used to measure permeability using the equipment and technique described in Boitnott (1997). A single-frequency sinusoid was employed as the primary transient. Frequency was tuned to optimize signal to noise for each sample. An asymmetrical spike transient (Boitnott, 1997) was used as backup in case an increase in permeability due to sample crushing occurred, but it was not needed for this suite of samples.

The samples were first pressurized to ~5 MPa effective confining pressure (confining pressure of 10 MPa and pore pressure of 5 MPa) and allowed to equilibrate to that stress. Permeability measurements were then performed, and appropriate measurement settings were selected. An automated measurement script was then run to perform the tests, making measurements of permeability at various points during loading and unloading. After each step increase or decrease in pressure, the controlled pressures were maintained constant and the downstream pressure was monitored until the effects of time-dependent compaction and pore pressure equilibration had passed. The pressure history for each sample is provided in Table T1.

Frequency-dependent electrical properties were measured using a Z-Meter impedance analysis system. A four-electrode configuration was used, and data were collected at frequencies ranging from 0.1 to 10000 Hz. Reported formation factors were compensated for small changes in temperature (typically a few degrees Celsius) resulting from adiabatic heating and cooling of the confining oil due to changes in confining pressure by correcting the brine conductivity measured at standard temperature (25°C) using the Arps (1953) empirical relationship for NaCl brines. Pore fluid temperature was monitored by a thermocouple located in the pore pressure tubing at the top of the sample.

T1. Permeability and resistivity measurements, p. 13.

G.J. Iturrino et al.
Data Report: Permeability, Resistivity, and CT Measurements

3

X-Ray Computed Tomography Measurements

X-ray computed tomography (CT) produces images in which gray-scale corresponds to the X-ray linear attenuation coefficient, which is primarily a function of density and atomic number. Individual CT images are referred to as slices because they correspond to what would be observed if an object were sliced open along the scan plane. By acquiring a contiguous set of slices, data for a complete volume can be obtained. The fundamental CT data unit is the voxel, or volume element, which corresponds to the volume bounded by the edges of a pixel and the thickness of the slice image. The CT value of a voxel is ideally a function of the attenuation coefficient of the material enclosed within it, although unavoidable blurring causes surrounding material to also have an influence.

If a voxel contains void space, its measured CT value will be a weighted average of the end-member values for air and the remaining material. If a fluid replaces the air, the net attenuation will rise due to the fluid being more attenuating than air; the increase in CT value is proportional to the percentage of void space. A map of the distribution of effective porosity can thus be created by imaging a sample twice, once each with pore space empty and filled, and subtracting the two data sets from each other.

All scanning was performed at the High-Resolution X-Ray CT facility at the University of Texas at Austin (UTCT), Texas (USA), and is described in detail by Ketcham and Carlson (2001). The X-ray source is a 200-kV FeinFocus model FXE200.20, which is capable of a <10-µm focal spot size. The detector system is an image intensifier from which data are captured and digitized by a charge-coupled device (CCD) camera. Subsequent to the description by Ketcham and Carlson (2001), the camera has been upgraded from one with 512 pixel × 512 pixel resolution to one with 1024 pixel × 1024 pixel resolution. Additionally, new computer hardware and software enable collection of data for multiple slices during a single rotation by utilizing data off the true horizontal plane used for standard scanning. Commonly, there is a distortion with increasing distance from the horizontal plane, which is most readily observed as a misfit between adjacent sets of slices from different rotations. However, the distortion attained with the UTCT system is negligible if the amount of the off-plane data utilized is restricted to the 25–30 video lines surrounding horizontal.

In the two-stage scanning protocol, each specimen was first dried for at least 1 day in a warm (~38°C) oven, weighed, and then scanned. The specimen was then infiltrated under vacuum with distilled water, weighed after excess water was removed with an absorbent tissue, and quickly scanned while still wet. The sample-mounting container was only marginally water-tight, and thus samples were wrapped in parafilm to restrict leakage. There was occasional slight drainage due to this protocol, and analyses would be improved by fabrication of water-tight sample mounts that precisely match the sample diameters. The maximum drainage inferred from mass loss of water during scanning was <0.1% of the fluid.

All the minicores were scanned with an X-ray peak energy of 150 kV and a current ranging between 0.21 and 0.25 mA. Each rotation consisted of 1000 views or angular positions, with an acquisition time of 0.133 s per view. Slices were two CCD camera pixel rows thick (57.8 µm), and 13–15 slices were acquired per rotation. A 24-mm field of reconstruction was captured in a 512 pixel × 512 pixel image. Between

250 and 425 slices were gathered, depending on sample size. Total data acquisition times were on the order of 2 hr per scan.
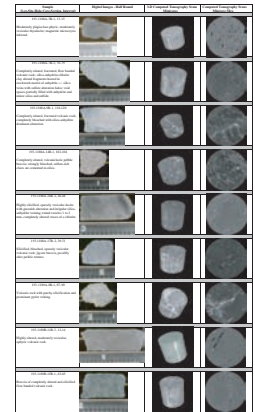
An important aspect of the scanning protocol was the use of a wedge calibration (Ketcham and Carlson, 2001), which consists of a set of detector readings through a full rotation of a material with identical geometry and similar attenuation properties as the material being scanned. By ensuring that the hardness of X-rays measured during calibration is similar to the beam hardness encountered during scanning, an appropriate wedge calibration is an effective solution for both beam hardening and a number of related issues, such as ring artifacts that stem from utilizing a polychromatic X-ray source. The wedge material used in this study was a core of pure synthetic quartz of identical diameter to the minicores. It is also possible to derive a software beam-hardening correction to detector readings (e.g., Clausnitzer and Hopmans, 2000), although these may be less effective at eliminating ring artifacts.

Larger half-round samples corresponding to the minicores were also scanned, although their non-cylindrical geometry prevented the employment of a proper wedge calibration to reduce beam-hardening artifacts sufficiently for the two-stage protocol to be used. Accordingly, these images were primarily intended for general visualization and comparison with the minicore images and visualizations. These visualizations document the loss in resolution when scanning larger samples and increasing the imaged volume. Scanning conditions were similar to those employed for the minicores, except the slice thickness was 127 μm and the field of reconstruction was 59 mm.

Three-dimensional (3-D) visualizations were created from the stacks of CT images using the software VG Studio Max (Volume Graphics GmbH, Germany). The software implements a visualization algorithm known as volume rendering, in which each voxel is assigned a color and opacity, allowing parts of the volume to be rendered fully or partially transparent. Three renderings were made for each sample scanned: one was made of the entire sample, one was made of the void space, and one was made of the high-density "bright" phases in the CT images. The images of the entire samples show the CT gray-level data rendered in 3-D. The void images highlight the larger pores, where CT gray levels are reliably below the levels for solid material. Large, open pores are opaque, whereas smaller pores that do not achieve as dark a gray level due to blurring with matrix are semi-transparent. For the minicores, the scans of the non-infiltrated samples were used, and microporosity detected by the two-stage scanning process was not included in these images so that they would be consistent with the visualizations of the half-rounds, for which such data were not available. In general, volume renderings of the partial-porosity data revealed by two-pass scanning were opaque and uninformative. The high-density phase visualizations often reveal at least two phases, with the higher-attenuation phase in yellow and the lower-attenuation phase in orange; however, in some cases the yellow phases have orange borders due to blurring or diffuse boundaries.

The color and opacity tables used to generate all of the renderings (Figs. F1, F2) are similar within each category but were manually adjusted using an interactive tool to improve the clarity of the visualization for each sample. The most significant adjustments made were to the opacity table where, if too much material is opaque, the visualization appears as a solid block, which is uninformative if the general purpose is to discern internal features. In all cases these images are meant to be illustrative, giving a sense of the distribution and character of the

F1. Digital core images, 3-D X-ray renditions, and examples of single slices, p. 8.

F2. 3-D X-ray computed tomography scans, p. 9.

G.J. Iturrino et al.
Data Report: Permeability, Resistivity, and CT Measurements

5
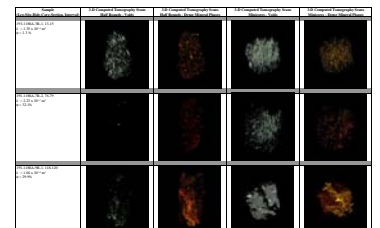
various components of interest. They are not quantitative, particularly in the case of void space, owing to the size range of the components of interest. More quantitative images of porosity are provided in a separate manuscript (Ketcham and Iturrino, in press).

PRELIMINARY RESULTS

In general, minicore permeabilities range from 10^{-17} to 10^{-14} m^2 and porosities were relatively high (Fig. F3A, F3B; Table T1). The values cited in this study are representative of similar permeability and porosity measurements from the PACMANUS hydrothermal system (Christiansen and Iturrino, this volume). The effect of pressure on both the measured permeabilities and electrical resistivities was small (Fig. F3A, F3C), except in the softer and more fragile samples where permanent deformation occurred. Deformation is apparent in samples where there is a significant deviation in measurements for equivalent increasing and decreasing pressure intervals (Fig. F3A; Table T1). The variations in electrical resistivity seem to be related to variations in porosity, where highly porous samples tend to be more conductive (Table T1).

A comparison of digital core images with minicore slice scans and 3-D X-ray tomography reconstructions shows clear evidence for variations in mineralogy, size and distribution of vesicles, vein distributions and orientations, and patchy alteration features (Fig. F1). Color renditions of 3-D X-ray tomography reconstructions also show distinct variations in distribution of dense phases and voids (Fig. F2). In some cases, the 3-D void renditions seem to correlate with porosity values obtained from minicore wet and dry weights and volumes, whereas in other instances, the porosity values seem low relative to the 3-D X-ray tomography void renditions. These variations are typically due to the range of pore sizes, as discussed above: large pores are opaque, whereas smaller pores will be partially or fully transparent.

A particularly interesting case is presented by Sample 193-1188A-3R-1, 13–15 cm, where the minicore porosity value is low and both the visual void rendition and permeability are high (Fig. F2). The grain and bulk density values show small variance (Table T1), supporting the low porosity and high electrical resistivity measurements. The CT visualization is somewhat deceptive, as the voids are large and open and thus opaque, and there are enough of them to seem to cover the sample space. Calculations from the CT data for the uninfiltrated minicore show that the vesicles compose ~5% of the sample by volume, but that many of these are not connected with the outside of the sample and were not filled when the sample was saturated for permeability and CT analysis. Examination of the CT data for the infiltrated sample reveals that its very high permeability can be traced to a single open conduit of connected vesicles that links the top and bottom surfaces of the minicore. Although this conduit is volumetrically small, it is wide enough that it offers comparatively little resistance to flow. However, it should also be noted that this conduit must have eventually terminated within the larger rock volume from which it was cut, and that if a larger sample without through-going conduits had been tested for permeability, presumably the results would have been different.

Sample 193-1188A-9R-1, 118–120 cm, is another case in which seemingly unusual porosity/permeability determinations may be explained by CT data. The permeability is lower than expected given the measured porosity, as compared with other samples in the suite that have

F3. Permeability, porosity, and resistivity, p. 12.
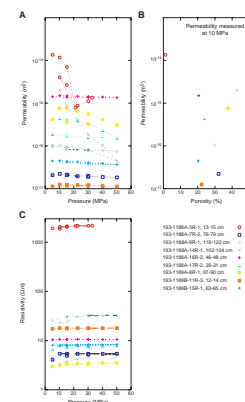
lower porosities and higher permeabilities. Examination of the 3-D visualization from the minicore shows that there are several sulfide veins surrounded by quartz, which were shown by two-stage scanning to be largely impermeable and thus may create effective barriers to flow. Two of these veins crosscut much of the minicore sample, likely causing a bottleneck during permeability determination and lowering measured values. The CT data for the corresponding half-round sample shows that these veins are distributed heterogeneously throughout the larger specimen, suggesting that the permeability in this lithology is locally variable, and that the determination for the minicore sample may be unrepresentative.

Significant variations in bright phases are observed in the 3-D X-ray tomography images, suggesting the potential for mineral identification and measurement. However, no direct mineral analyses on cores have been made at this point to verify the accuracy of these images or to identify the particular phases imaged in each sample. Mineral identification in CT data typically relies on some prior knowledge of the phases expected to be present (e.g., Carlson and Denison, 1992; Orsi et al., 1994; Tivey, 1998), although in some cases dual-energy scanning can be used to derive atomic number information, giving additional clues as to composition (Van Geet et al., 2000). If phases or voids can be successfully identified and segmented within the CT data volume, specialized software can be employed to obtain 3-D measurements of size, shape, distribution, and orientation (Kyle and Ketcham, 2004, with supplementary material available at **www.ctlab.geo.utexas.edu/pubs/kyle&ketcham/k&k.htm;** Proussevitch and Sahagian, 2001).

ACKNOWLEDGMENTS

REFERENCES

Arps, J.J., 1953. The effect of temperature on the density and electrical resistivity of sodium chloride solutions. *Trans. AIME,* 98:327–328.

Binns, R.A., Barriga, F.J.A.S., Miller, D.J., et al., 2002. *Proc. ODP, Init. Repts.,* 193 [CD-ROM]. Available from: Ocean Drilling Program, Texas A&M University, College Station TX 77845-9547, USA.

Boitnott, G.N., 1997. Use of complex pore pressure transients to measure permeability of rocks. *Pap. Conf.—Soc. Pet. Eng. AIME,* 38717:37–45.

Carlson, W.D., and Denison, C., 1992. Mechanisms of porphyroblast crystallization: results from high-resolution computed X-ray tomography. *Science,* 257:1236–1239.

Clausnitzer, V., and Hopmans, J.W., 2000. Pore-scale measurements of solute breakthrough using microfocus X-ray computed tomography. *Water Resour. Res.,* 36:2067–2079.

Jacobson, R.S., 1992. The impact of crustal evolution on changes of the seismic properties of the uppermost ocean crust. *Rev. Geophys.,* 30:23–42.

Johnson, H.P., and Semyan, S.W., 1994. Age variation in the physical properties of oceanic basalts: implications for crustal formation and evolution. *J. Geophys. Res.,* 99:3123–3134.

Ketcham, R.A., and Carlson, W.D., 2001. Acquisition, optimization and interpretation of X-ray computed tomographic imagery: applications to the geosciences. *Comput. Geosci.,* 27:381–400.

Ketcham, R.A., and Iturrino, G.J., in press. Nondestructive high-resolution visualization and measurement of anisotropic effective porosity in complex lithologies using high-resolution X-ray computed tomography. *J. Hydrol. (Amsterdam, Neth.).*

Kyle, J.R., and Ketcham, R.A., 2004. In-situ distribution of gold ores using high-resolution X-ray computed tomography. *Econ. Geol.,* 98:1697–1701.

Orsi, T.H., Edwards, C.M., and Anderson, A.L., 1994. X-ray computed tomography: a nondestructive method for quantitative analysis of sediment cores. *J. Sediment. Res.,* A64:690–693.

Proussevitch, A., and Sahagian, D., 2001. Recognition and separation of discrete objects within complex 3D voxelized structures. *Comput. Geosci.,* 27:441–454.

Thompson, G., 1983. Basalt-seawater interaction. *In* Rona, P.A., Boström, K., Laubier, L., and Smith, K.L., Jr. (Eds.), *Hydrothermal Processes at Seafloor Spreading Centers:* New York (Plenum), 225–278.

Tivey, M.K., 1998. Documenting textures and mineral abundances in minicores from the TAG active hydrothermal mound using X-ray computed tomography. *In* Herzig, P.M., Humphris, S.E., Miller, D.J., and Zierenberg, R.A. (Eds.), *Proc. ODP, Sci. Results,* 158: College Station, TX (Ocean Drilling Program), 201–210.

Van Geet, M., Swennen, R., and Wevers, M., 2000. Quantitative analysis of reservoir rocks by microfocus X-ray computerised tomography. *Sediment. Geol.,* 132:25–36.

Figure F1. Digital core images, 3-D X-ray computed tomography minicore renditions, and examples of the single slices used for the 3-D displays.
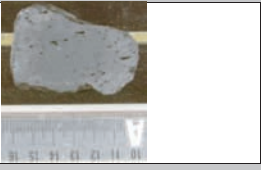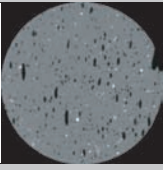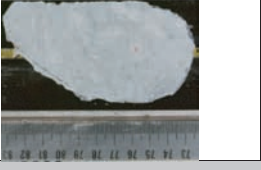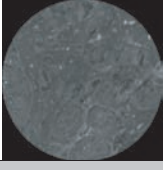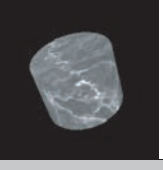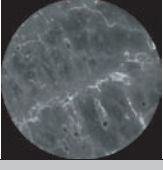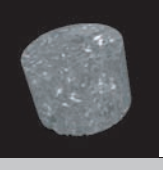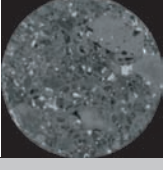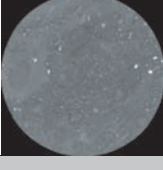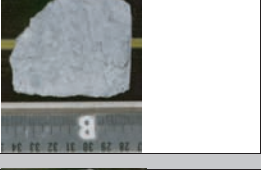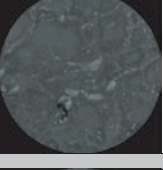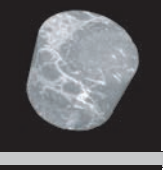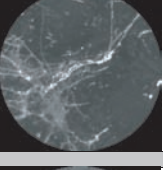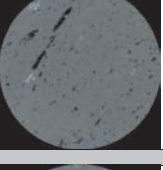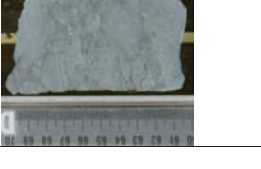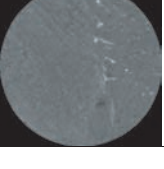
Sample (Leg-Site-Hole-Core-Section, Interval)	Digital Images - Half Round	3-D Computed Tomography Scans Minicores	Computed Tomography Scans Minicore Slice
193-1188A-3R-1, 13-15 Moderately plagioclase-phyric, moderately vesicular rhyodacite; magnetite microcrysts inferred.			
193-1188A-7R-2, 76-79 Completely altered, fractured, flow banded volcanic rock; silica-anhydrite-chlorite clay altered fragments hosted in stockwork matrix of anhydrite +/- silica veins with sulfate alteration halos; void spaces partially filled with anhydrite and minor silica and sulfide.			
193-1188A-9R-1, 118-120 Completely altered, fractured volcanic rock; completely bleached with silica-anhydrite dominant alteration.			
193-1188A-14R-1, 102-104 Completely altered, volcaniclastic pebble breccia; strongly bleached, sulfate-rich clasts are cemented in silica.			
193-1188A-16R-2, 46-48 Highly silicified, sparsely vesicular dacite with greenish alteration and irelgular silica-anhydrite veining; round vesicles 1 to 2 mm, completely altered; traces of a chlorite.			
193-1188A-17R-2, 29-31 Silicified, bleached, sparsely vesicular volcanic rock; jigsaw breccia, possibly after perlitic texture.			
193-1189A-8R-1, 87-90 Volcanic rock with patchy silicification and prominent pyrite veining.			
193-1189B-11R-3, 12-14 Highly altered, moderately vesicular, aphyric volcanic rock.			
193-1189B-15R-1, 63-65 Breccia of completely altered and silicified flow banded volcanic rock.			

Figure F2. 3-D X-ray computed tomography scans of half rounds and minicores taken from the same intervals. k = permeability measured at 5 MPa confining pressure, ϕ = porosity at atmospheric pressure. All images are based on dry measurements. (Continued on next two pages.)

Sample (Leg-Site-Hole-Core-Section, Interval)	3-D Computed Tomography Scans Half Rounds - Voids	3-D Computed Tomography Scans Half Rounds - Dense Mineral Phases	3-D Computed Tomography Scans Minicores - Voids	3-D Computed Tomography Scans Minicores - Dense Mineral Phases
193-1188A-3R-1, 13-15 k = 1.35 x 10^{-14} m^2 ϕ = 1.3 %				
193-1188A-7R-2, 76-79 k = 2.23 x 10^{-17} m^2 ϕ = 32.1%				
193-1188A-9R-1, 118-120 k = 1.04 x 10^{-16} m^2 ϕ = 29.9%				

Figure F2 (continued).
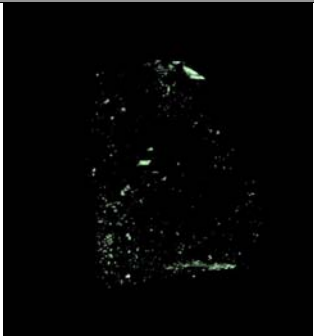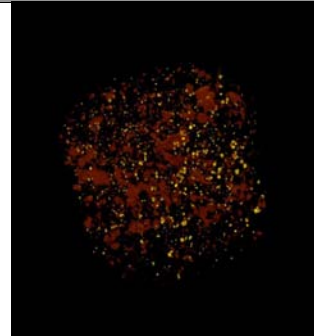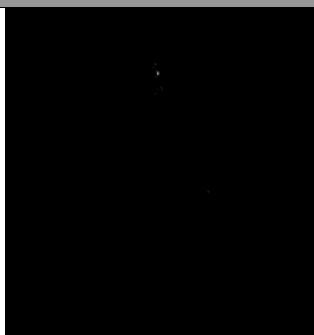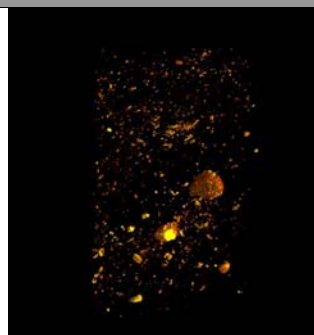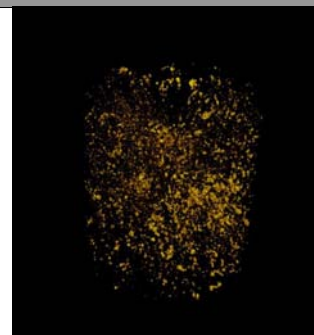
Sample (Leg-Site-Hole-Core-Section, Interval)	3-D Computed Tomography Scans Half Rounds - Voids	3-D Computed Tomography Scans Half Rounds - Dense Mineral Phases	3-D Computed Tomography Scans Minicores - Voids	3-D Computed Tomography Scans Minicores - Dense Mineral Phases
193-1188A-14R-1, 102-104 $k = 2.00 \times 10^{-15}$ m^2 $\phi = 42.7\%$				
193-1188A-16R-2, 46-48 $k = 1.50 \times 10^{-15}$ m^2 $\phi = 20.6\%$				
193-1188A-17R-2, 29-31 $k = 4.46 \times 10^{-16}$ m^2 $\phi = 24.0\%$				

Figure F2 (continued).
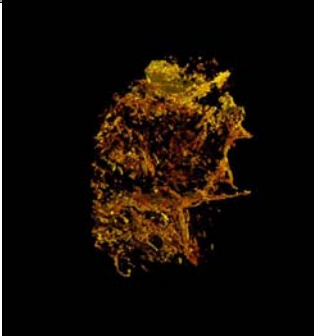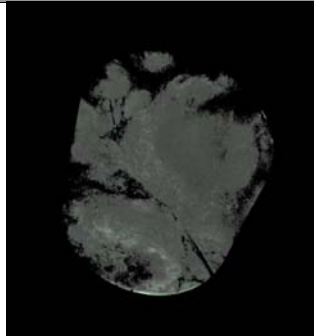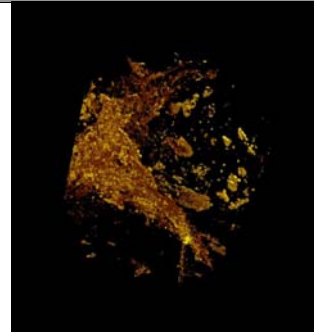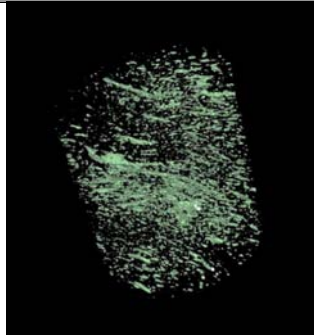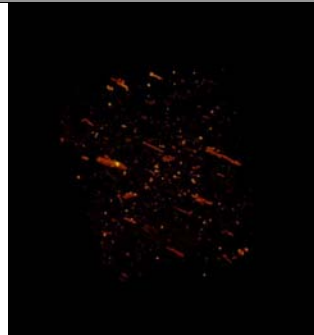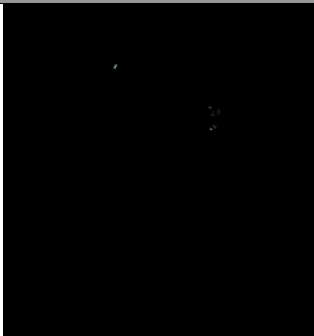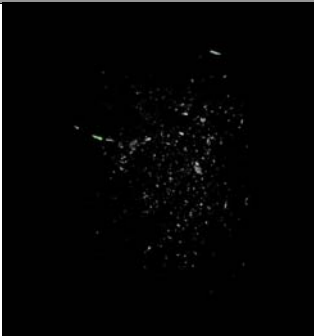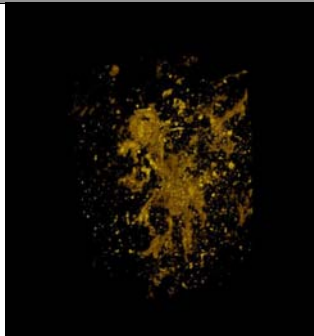
G.J. Iturrino et al.
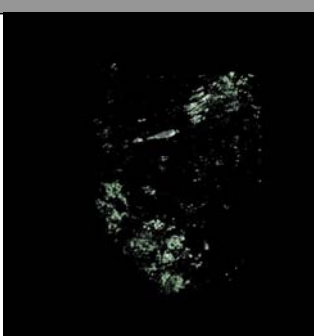Data Report: Permeability, Resistivity, and CT Measurements
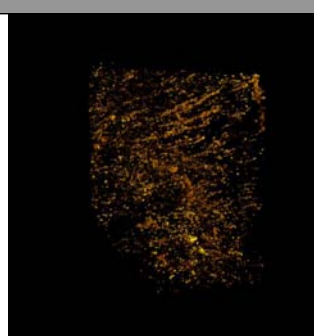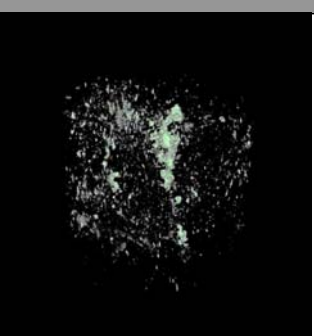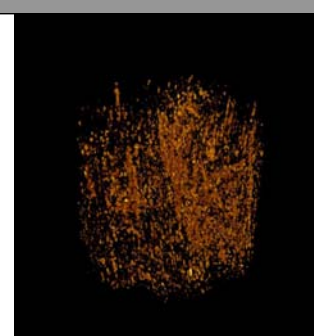
11

Sample (Leg-Site-Hole-Core-Section, Interval)	3-D Computed Tomography Scans Half Rounds - Voids	3-D Computed Tomography Scans Half Rounds - Dense Mineral Phases	3-D Computed Tomography Scans Minicores - Voids	3-D Computed Tomography Scans Minicores - Dense Mineral Phases
193-1189A-8R-1, 87-90 k = 7.59 x 10^{-16} m^2 ϕ = 37.6%	Image is not available because the voids were too small to be imaged and reliably distinguished from matrix at this resolution.			
193-1189B-11R-3, 12-14 k = 1.25 x 10^{-17} m^2 ϕ = 22.2%				
193-1189B-15R-1, 63-65 k = 4.48 x 10^{-17} m^2 ϕ = 20.3%				

Figure F3. A. Permeability measurements as a function of confining pressure for minicore samples from the Snowcap and Roman Ruins hydrothermal fields. **B.** Porosity and permeability relationship for the same minicore samples. **C.** Resistivity measurements as a function of pressure for minicore samples.

Table T1. Results from permeability and resistivity measurements at different confining pressures. (Continued on next page.)

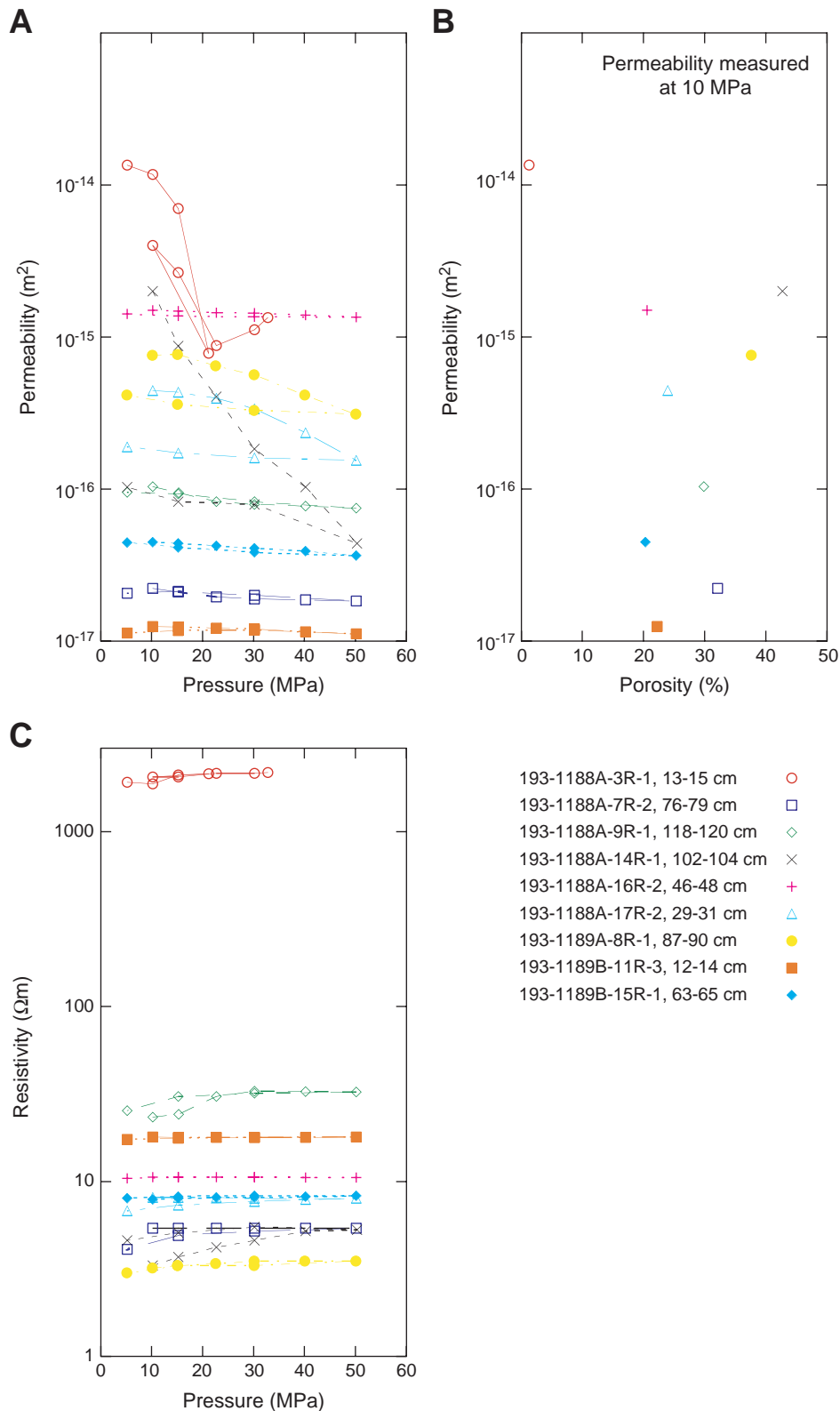| Core, section, interval (cm), properties	Pressure (MPa)	Permeability (m²)	Resistivity (Ωm)	Formation factor	Comments

193-1188A-3R-1, 13–15
  Water depth = 1640.2 mbsl
  Sample depth = 19.33 mbsf
  Porosity = 1.3%
  Bulk density = 2.335 g/cm³
  Grain density = 2.341 g/cm³
	5.2
	10.2
	15.2
	21.2
	10.2
	15.2
	22.7
	30.2
	32.8
	32.7
	30.2
	15.2
	5.2
		1.35E–14
		1.17E–14
		6.99E–15
		7.84E–16
		4.00E–15
		2.65E–15
		8.81E–16
		1.12E–15
		1.34E–15
		1.24E–15
		1.66E–15
		1.97E–15
		1.87E–14
			1920.0
			1872.0
			2107.0
			2146.0
			2056.0
			2053.0
			2151.0
			2158.0
			2171.0
			2224.0
			2206.0
			2110.0
			2047.0
				542.4
				525.8
				591.9
				599.4
				584.1
				578.4
				597.5
				601.1
				606.4
				610.9
				609.3
				590.9
				576.5
					Moderately plagioclase-phyric, moderately vesicular rhyodacite; magnetite microcrysts inferred.

198-1188A-7R-2, 76–79
  Water depth = 1640.2 mbsl
  Sample depth = 50.46 mbsf
  Porosity = 32.1%
  Bulk density = 2.07 g/cm³
  Grain density = 2.55 g/cm³
	10.2
	15.2
	22.7
	30.2
	40.2
	50.2
	30.2
	15.2
	5.2
		2.23E–17
		2.10E–17
		1.95E–17
		1.89E–17
		1.87E–17
		1.84E–17
		2.00E–17
		2.12E–17
		2.07E–17
			5.4
			5.4
			5.4
			5.4
			5.4
			5.4
			5.2
			4.9
			4.1
				19.4
				19.6
				19.6
				19.5
				19.5
				19.8
				19.0
				17.7
				14.7
					Completely altered, fractured, flow-banded volcanic rock; silica-anhydrite-chlorite clay altered fragments hosted in stockwork matrix of anhydrite silica veins with sulfate alteration halos; void spaces partially filled with anhydrite and minor silica and sulfide.

193-1188A-9R-1, 118–120
  Water depth = 1640.2 mbsl
  Sample depth = 68.78 mbsf
  Porosity = 29.9%
	10.2
	15.3
	22.7
	30.2
	40.2
	50.2
	30.2
	15.2
	5.2
		1.04E–16
		9.47E–17
		8.29E–17
		7.90E–17
		7.76E–17
		7.49E–17
		8.27E–17
		9.28E–17
		9.54E–17
			23.3
			24.2
			30.7
			32.8
			32.6
			32.5
			32.0
			30.6
			25.4
				6.0
				6.2
				6.3
				6.3
				6.3
				6.3
				6.2
				6.0
				5.6
					Completely altered, fractured volcanic rock; completely bleached with silica-anhydrite dominant alteration.

193-1188A-14R-1, 102–104
  Water depth = 1640.2 mbsl
  Sample depth = 117.02 mbsf
  Porosity = 42.7%
  Bulk density = 2.03 g/cm³
  Grain density = 2.71 g/cm³
	10.2
	15.2
	22.7
	30.2
	40.2
	50.3
	30.2
	15.2
	5.2
		2.00E–15
		8.74E–16
		4.05E–16
		1.84E–16
		1.03E–16
		4.41E–17
		7.93E–17
		8.28E–17
		1.03E–16
			3.3
			3.7
			4.2
			4.6
			5.2
			5.3
			5.5
			5.1
			4.6
				12.3
				13.6
				15.5
				17.1
				19.2
				19.7
				19.9
				18.5
				16.7
					Completely altered, volcaniclastic pebble breccia; strongly bleached, sulfate-rich clasts are cemented in silica.

193-1188A-16R-2, 46–48
  Water depth = 1640.2 mbsl
  Sample depth = 137.36 mbsf
  Porosity = 20.6%
  Bulk density = 2.39 g/cm³
  Grain density = 2.69 g/cm³
	10.2
	15.2
	22.7
	30.2
	40.2
	50.2
	30.2
	15.2
	5.2
		1.50E–15
		1.48E–15
		1.45E–15
		1.44E–15
		1.39E–15
		1.35E–15
		1.36E–15
		1.38E–15
		1.42E–15
			10.6
			10.6
			10.6
			10.6
			10.5
			10.5
			10.6
			10.6
			10.4
				38.6
				38.7
				38.8
				38.9
				38.8
				38.7
				38.3
				37.9
				37.6
					Highly silicified, sparsely vesicular dacite with greenish alteration and irregular silica-anhydrite veining; round vesicles 1 to 2 mm, completely altered; traces of a chlorite.

193-1188A-17R-2, 29–31
  Water depth = 1640.2 mbsl
  Sample depth = 146.89 mbsf
  Porosity = 24.0%
  Bulk density = 2.33 g/cm³
  Grain density = 2.71 g/cm³
	10.2
	15.2
	22.7
	30.2
	40.2
	50.2
	30.2
	15.2
	5.2
		4.46E–16
		4.34E–16
		3.97E–16
		3.38E–16
		2.35E–16
		1.55E–16
		1.60E–16
		1.73E–16
		1.89E–16
			8.1
			8.1
			8.1
			8.0
			7.9
			8.0
			7.7
			7.3
			6.8
				28.8
				28.8
				28.7
				28.5
				28.8
				29.0
				27.6
				26.2
				24.4
					Silicified, bleached, sparsely vesicular volcanic rock; jigsaw breccia, possibly after perlitic texture.

Table T1 (continued).

Core, section, interval (cm), properties	Pressure (MPa)	Permeability (m²)	Resistivity (Ωm)	Formation factor	Comments
193-1189A-8R-1, 87–90	10.1	7.59E–16	3.2	12.2	Volcanic rock with patchy silicification and prominent pyrite veining.
Water depth = 1690.2 mbsl	15.1	7.69E–16	3.3	12.5	
Sample depth = 68.87 mbsf	22.6	6.45E–16	3.4	12.9	
Porosity = 37.6%	30.1	5.66E–16	3.5	13.3	
Bulk density = 2.06 g/cm³	40.1	4.15E–16	3.5	13.6	
Grain density = 2.69 g/cm³	50.1	3.11E–16	3.5	13.6	
	30.1	3.29E–16	3.3	12.3	
	15.1	3.61E–16	3.3	12.2	
	5.1	4.15E–16	3.0	10.9	
193-1189B-11R-3, 12–14	10.2	1.25E–17	18.0	55.6	Highly altered, moderately vesicular, aphyric volcanic rock.
Water depth = 1681.7 mbsl	15.2	1.24E–17	17.9	55.5	
Sample depth = 130.72 mbsf	22.7	1.22E–17	17.9	56.4	
Porosity = 22.2%	30.2	1.20E–17	17.9	57.0	
	40.2	1.15E–17	17.9	58.0	
	50.2	1.12E–17	18.0	58.2	
	30.2	1.18E–17	17.9	56.7	
	15.2	1.17E–17	17.7	55.8	
	5.2	1.13E–17	17.4	55.1	
193-1189B-15R-1, 63–65	10.2	4.48E–17	7.9	29.4	Breccia of completely altered and silicified flow-banded volcanic rock.
Water depth = 1681.7 mbsl	15.2	4.40E–17	8.0	29.7	
Sample depth = 166.73 mbsf	22.7	4.24E–17	8.1	30.1	
Porosity = 20.3%	30.2	4.08E–17	8.1	30.4	
	40.2	3.91E–17	8.2	30.6	
	50.2	3.65E–17	8.3	31.1	
	30.2	3.85E–17	8.3	30.5	
	15.2	4.13E–17	8.2	29.9	
	5.2	4.45E–17	8.0	29.3	